REPORT DOCUMENTATION PAGE

Form Approved
OMB No. 0704-0188

1. AGENCY USE ONLY *(Leave blank)*	2. REPORT DATE	3. REPORT TYPE AND DATES COVERED
	April 1992	Technical Memorandum

4. TITLE AND SUBTITLE
Longitudinal and Lateral-Directional Aerodynamic Characteristics of a Wing-Cone Configuration at Mach Numbers From 2.5 to 4.5

5. FUNDING NUMBERS
WU 505-61-31-08

6. AUTHOR(S)
Peter F. Covell, Ira J. Walker, and Dorothy T. Howell

7. PERFORMING ORGANIZATION NAME(S) AND ADDRESS(ES)
NASA Langley Research Center
Hampton, VA 23665-5225

8. PERFORMING ORGANIZATION REPORT NUMBER
L-16839

9. SPONSORING/MONITORING AGENCY NAME(S) AND ADDRESS(ES)
National Aeronautics and Space Administration
Washington, DC 20546-0001

10. SPONSORING/MONITORING AGENCY REPORT NUMBER
NASA TM-4337

11. SUPPLEMENTARY NOTES
Covell and Howell: Langley Research Center, Hampton, VA; Walker: Lockheed Engineering & Sciences Company, Hampton, VA.

12a. DISTRIBUTION/AVAILABILITY STATEMENT
Unclassified–Unlimited

Subject Category 02

12b. DISTRIBUTION CODE

13. ABSTRACT *(Maximum 200 words)*
An investigation has been conducted to determine the longitudinal and lateral-directional aerodynamic characteristics of a generic wing-cone configuration at supersonic speeds. The fuselage had a 5° half-angle cone forebody, cylindrical midbody, and a 9° truncated cone afterbody. The delta wing (aspect ratio 1.0) had a 4-percent-thick diamond airfoil section. The tests were made in the Langley Unitary Plan Wind Tunnel at Mach numbers from 2.50 to 4.50. Angle of attack was varied from −4° to 28°, and angle of sideslip varied from −8° to 8°. Several configurations were studied to determine the effects of variations in wing longitudinal position, wing incidence, vertical-tail configuration, canard shape, and nose bluntness. Typical effects of Reynolds number and Mach number on the longitudinal characteristics were observed. The incremental effects of the confiuration variables were generally unaffected by Mach number. The directional-stability characteristics of the large and small centerline-mounted vertical-tail configurations were significantly degraded with increasing angle of attack and Mach number.

14. SUBJECT TERMS
Supersonic aerodynamics; Lateral-directional aerodynamics; Conical forebody; Longitudinal aerodynamics

15. NUMBER OF PAGES
174

16. PRICE CODE
A08

17. SECURITY CLASSIFICATION OF REPORT	18. SECURITY CLASSIFICATION OF THIS PAGE	19. SECURITY CLASSIFICATION OF ABSTRACT	20. LIMITATION OF ABSTRACT
Unclassified	Unclassified		

NSN 7540-01-280-5500

Standard Form 298(Rev. 2-89)
Prescribed by ANSI Std. Z39-18
298-102

NASA-Langley, 1992

Summary

An investigation has been conducted to determine the longitudinal and lateral-directional aerodynamic characteristics of a generic wing-cone configuration at supersonic speeds. The tests were made in the Langley Unitary Plan Wind Tunnel at Mach numbers from 2.50 to 4.50. Nominal test Reynolds number based on body length was 6×10^6, with selected runs made at 3 and 12×10^6. Angle of attack was varied from $-4°$ to $28°$, and angle of sideslip was varied from $-8°$ to $8°$. Several configurations were studied to determine the effects of variations in wing longitudinal position, wing incidence, vertical-tail configuration, canard shape, and nose bluntness.

Typical effects of Reynolds number and Mach number on the longitudinal characteristics were observed. The incremental effects of the configuration variables were generally unaffected by Mach number. Forward wing shift was found to have a favorable effect on the lift and drag-due-to-lift characteristics. Wing incidence yielded nearly constant shifts in normal force, lift, and pitch at low angles of attack. The wing-mounted twin vertical tails increased the stability level, the normal-force-curve slope, and the lift-curve slope.

The directional-stability characteristics of the large and small centerline-mounted vertical-tail configurations were significantly degraded with increasing angle of attack and Mach number. The wing-mounted vertical tails provided near-neutral directional stability across the test angle-of-attack range. Generally, all configurations were laterally stable for positive angles of attack. Lateral-directional asymmetries occurred at zero sideslip for angles of attack above $20°$ for the centerline vertical-tail configurations.

Introduction

The wing-cone configuration has been identified as a potential transatmospheric vehicle candidate. One advantageous feature of the wing-cone configuration is that the inlets can be distributed around the body circumference to maximize inlet capture area. In addition, the conical forebody provides an initial precompression surface for the inlet flow field. The circular body cross section also provides both structural and fuel-volume efficiency. Finally, the geometric simplicity of the wing-cone configuration makes it readily amenable to analysis with a broad range of computational aerodynamic prediction methods.

The objective of the present research effort was to define the aerodynamic characteristics of a generic wing-cone configuration in the Mach 2.50 to 4.50 speed range. Several configuration variables were studied to provide trade information on wing longitudinal position, wing incidence, vertical-tail configuration, canard shape, and nose bluntness effects. A preliminary assessment of the test results has been reported in reference 1. Subsonic tests of the configuration have been reported in references 2–5.

The wing-cone model was tested in the NASA Langley Unitary Plan Wind Tunnel (UPWT) at Mach numbers from 2.50 to 4.50 for Reynolds numbers from 3 to 12×10^6 based on body length. The angle of attack was varied from $-4°$ to $28°$ and angle of sideslip was varied from $-8°$ to $8°$ for selected angles of attack.

Symbols

The aerodynamic coefficients are referred to the body-axis system unless otherwise noted. Lift and drag are referred to the stability-axis system. The data were reduced about a moment reference center located at 62 percent of the fuselage length. (See fig. 1(a).)

b	wingspan, 10.80 in.
$\bar{c}$	mean aerodynamic chord, 14.40 in.
C_A	axial-force coefficient, $\frac{\text{Axial force}}{qS}$
$C_{A,c}$	chamber axial-force coefficient, $\frac{\text{Chamber axial force}}{qS}$
C_D	drag coefficient, $\frac{\text{Drag}}{qS}$
$C_{D,c}$	chamber drag coefficient, $\frac{\text{Chamber drag}}{qS}$
$C_{D,o}$	drag coefficient at zero lift
C_l	rolling-moment coefficient, $\frac{\text{Rolling moment}}{qSb}$
$C_{l,s}$	stability axis rolling-moment coefficient, $\frac{\text{Rolling moment}}{qSb}$
C_{l_β}	lateral-stability derivative, $\frac{(C_l)_{\beta=3} - (C_l)_{\beta=0}}{3}$
$\left(C_{l_\beta}\right)_s$	stability axis lateral-stability derivative, $\frac{(C_{l,s})_{\beta=3} - (C_{l,s})_{\beta=0}}{3}$
C_L	lift coefficient, $\frac{\text{Lift}}{qS}$
C_m	pitching-moment coefficient, $\frac{\text{Pitching moment}}{qS\bar{c}}$
C_n	yawing-moment coefficient, $\frac{\text{Yawing moment}}{qSb}$

$C_{n,s}$ stability axis yawing-moment coefficient, $\frac{\text{Yawing moment}}{qSb}$

C_{n_β} directional-stability derivative, $\frac{(C_n)_{\beta=3} - (C_n)_{\beta=0}}{3}$

$\left(C_{n_\beta}\right)_s$ stability axis directional-stability derivative, $\frac{(C_{n,s})_{\beta=3} - (C_{n,s})_{\beta=0}}{3}$

C_N normal-force coefficient, $\frac{\text{Normal force}}{qS}$

C_Y side-force coefficient, $\frac{\text{Side force}}{qS}$

C_{Y_β} side-force derivative, $\frac{(C_Y)_{\beta=3} - (C_Y)_{\beta=0}}{3}$

F.S. fuselage station

L body length, 36.00 in.

L/D lift-drag ratio

M free-stream Mach number

q free-stream dynamic pressure, psi

R Reynolds number, per ft

S wing reference area, 116.64 in^2

v variable

x_{CP}/L longitudinal location of center of pressure referenced to body length

α angle of attack, deg

β angle of sideslip, deg

δ_i wing incidence, deg

Configuration nomenclature:

B body

C1 delta canard

C2 trapezoidal canard

N3 blunt nose

N4 nose used with canards

N5 sharp nose

V1 large centerline-mounted vertical tail

V2 small centerline-mounted vertical tail

V3 wing-mounted vertical tails

W1 wing in baseline (mid) position at zero incidence

W1A wing in aft position at zero incidence

W1F wing in forward position at zero incidence

W1I wing in baseline (mid) position at nonzero incidence

Model Description

A sketch of the wing-cone model along with the various additional components is shown in figure 1. The baseline wing-cone model consists of a 5° half-angle cone forebody, cylindrical midbody, and a 9° truncated cone afterbody. Typically, an engine package would be located at the midbody; however, the engine package was deleted from the present model to simplify the experiment and analysis. The fuselage is fitted with a delta wing (aspect ratio 1.0) with a 4-percent-thick diamond airfoil section. The wing could be located at three longitudinal positions and five incidence angles. The model components included interchangeable nose geometries that varied in bluntness, two canards that differed in planform, and three vertical-tail configurations. The three vertical-tail configurations were large and small centerline-mounted and split wing-mounted arrangements. The sharp nose (designated N5) was used for the majority of the tests. The canard nose (N4) was intended to have the same geometry as N5. Geometric characteristics of the model components are summarized in table I.

A sketch showing the possible wing positions is presented in figure 1(f). The model was designed to allow the wing to be positioned at five incidence angles (−5°, −2.5°, 0°, 2.5°, and 5°) and three longitudinal positions while maintaining a smooth wing-body juncture. Wing incidence and position were studied to assess induced lift and wing-body interference effects. Also, wing incidence could be used to allow the forebody, which serves as an external surface for an inlet, to remain at a reduced angle of attack relative to free stream to minimize forebody cross flow into the inlet. A photograph of the baseline wing-cone model with the large centerline vertical tail is shown in figure 2.

Test Conditions

The tests were made in the NASA Langley UPWT. The UPWT is a variable pressure and temperature wind tunnel with a Mach number range from 1.5 to 4.6. The UPWT has two test sections; test section 1 has a Mach number range from 1.5 to 2.9 and test section 2 has a Mach number

range from 2.3 to 4.6. A complete description of the UPWT is contained in reference 6. Test section 2 was used for the present tests, which were made at Mach 2.50, 3.00, 3.50, 4.00, and 4.50. The nominal test Reynolds number was 2×10^6 per foot; however, selected tests were made at Reynolds numbers of 1×10^6 and 4×10^6 per foot. A detailed outline of the wind-tunnel test parameters is contained in table II.

Angle of attack was varied from $-4°$ to $28°$ at sideslip angles of $0°$ and $3°$. The angle of sideslip was varied from $-8°$ to $8°$ at selected angles of attack. Although typical transatmospheric vehicles would likely operate at angles of attack less than $10°$, tests were made at the higher angles to evaluate potential off-design abort or reentry conditions. A boundary-layer transition strip consisting of No. 35 grit was located 1.2 in. aft of the fuselage nose apex and 0.4 in. aft streamwise of the wing, canard, and vertical-tail leading edges. The grit size and location were selected according to the methods discussed in references 7–9.

The aerodynamic forces and moments were measured by means of a six-component strain-gauge balance contained within the model and attached to a support sting that, in turn, was connected to the permanent model-positioning system in the wind tunnel. The absolute balance accuracy was 0.5 percent of the full-scale capacity of each of the six balance components. The resultant coefficient accuracies for the various test conditions are contained in table III. The model angles of attack were corrected for tunnel flow misalignment and for sting and balance deflection caused by aerodynamic loading on the model. Balance chamber pressures were measured by means of sting-mounted tubes routed from inside the chamber to pressure transducers located outside the wind tunnel. These pressures were measured throughout the test and were used to correct the force data to a condition of free-stream static pressure acting over the base area of the model. The data were reduced about a moment reference center located at 62 percent of the model length.

Presentation of Results

The aerodynamic coefficient data are tabulated in the appendix. The data are plotted in figures 3 to 30. The data plot scales were sized to best illustrate the most important trends in the data. In certain instances (such as drag coefficient at large values of lift coefficient) the data points are off scale and hence are not plotted; however, these data points are included in the appendix. Unless otherwise indicated, the results presented in the following figures are for a Reynolds number of 2×10^6 per foot:

Summary of Results

Because of the large amount of experimental data obtained in the study, this paper will highlight only the most significant results. The longitudinal aerodynamic characteristics will be discussed first, followed by the lateral-directional characteristics. The baseline configuration used in the data comparisons is the wing-body configuration, with the wing located in the midposition at zero incidence (W1BN5).

Longitudinal Aerodynamic Characteristics

The effect of Reynolds number is shown in figures 3–5 for the body-alone (BN5), wing-body (W1BN5), and large centerline vertical-tail (W1BN5V1) configurations at Mach 2.50 and 4.50. Only the axial-force coefficient (C_A), drag coefficient (C_D), and lift-drag ratio (L/D) exhibit any noticeable effect. The expected decrease in C_A (and C_D) with increasing Reynolds number occurs for low angles of attack ($\alpha < 2°$); this trend generally does not hold for the higher angle-of-attack conditions.

Shown in figures 6–9 is the effect of Mach number on the body-alone (BN5), wing-body (W1BN5), large centerline vertical tail (W1BN5V1), and delta canard (W1BN4C1) configurations. The following general trends were observed for increasing Mach number: stability level decreased, normal-force-curve and lift-curve slope decreased, zero-lift drag and axial force decreased, drag due to lift increased, and maximum lift-drag ratio increased. In the present study, drag due to lift is defined as $C_D - C_{D,o}$. The axial-force curves merged for angles of attack between 16° and 20°; at higher angles of attack, the axial force increased with increasing Mach number.

The effect of vertical-tail configuration is shown in figure 10. As expected, the axial force and drag increased and lift-drag ratio decreased because of the centerline-mounted vertical tails (V1 and V2). The wing-mounted vertical tails (V3) had the largest increments of axial force and zero-lift drag. However, the wing-mounted vertical tails also increased the stability level, the normal-force-curve slope, and the lift-curve slope. These results may be attributed to the vertical tails on the lower surface of the wing lower surface acting as a type of "flow fence" to capture the flow, and causing higher local pressures aft of the moment reference center. In addition, the wing-mounted vertical tails had the lowest drag due to lift, which resulted in slightly higher values of lift-drag ratio for lift coefficients above about 0.3.

The effect of the delta (C1) and trapezoidal (C2) canard configurations is shown in figure 11. The typical effects due to canard addition occur: stability level decreased, normal force and lift-curve slope increased, axial force and zero-lift drag increased, and drag due to lift decreased. The baseline wing-body configuration has the highest maximum lift-drag ratio. Both canard configurations have greater lift-drag ratio at the higher lift coefficients ($C_L > 0.15$–0.25) because of their lower drag due to lift than the baseline configuration.

The effect of wing longitudinal position is shown in figure 12. In addition to the expected destabilizing effect of forward wing shift, several additional effects occurred: normal force and lift-curve slope increased, axial force increased, drag due to lift decreased, and maximum lift-drag ratio increased. These additional effects may be attributed to changes in wing-on-body and body-on-wing interference effects. For example, forward wing movement places more of the wing in the forebody compression flow field and less of the wing in the afterbody expansion flow field.

Wing incidence effects are shown in figure 13. Positive wing incidence yields a near-constant negative pitch-curve shift and a near-constant positive normal-force-curve and lift-curve shift for angles of attack less than about 8°. Above this angle of attack, these incremental shifts generally increase. Large increments in axial force occur as angle of attack increases. Generally, the zero incidence (baseline wing-body) configuration has the largest maximum lift-drag ratio. For lift coefficients greater than 0.35, the drag increases as the wing incidence varies from positive to negative; this effect is more apparent as Mach number increases.

Varying the nose geometry from sharp (N5) to blunt (N3) was found to have minimal effect, except for the axial-force data at low angles of attack ($\alpha < 2°$) for Mach 4.00 and 4.50 (fig. 14). This effect may be due to skin friction reduction caused by laminar flow downstream of the transition grit on

the blunt nose; this hypothesis is based on the favorable effect of bluntness on transition Reynolds number (ref. 10) and the marginal effectiveness of the transition grit at Mach numbers above 4.00 (ref. 8). Also shown in figure 14 are the data for the body alone and the wing-body. The results show that the addition of the wing to the body at Mach 2.50 yields about a threefold increase in normal force or lift at low angles of attack ($\alpha < 8°$); at Mach 4.50 a twofold increase in normal force or lift occurs. This Mach number effect on the normal-force or lift increase due to wing addition can be attributed to two factors. Relative to the body-alone lift (which is nearly independent of Mach number at low angles of attack) both the isolated wing lift and the favorable (i.e., lift-producing) wing-body interference effects decrease significantly as Mach number increases (ref. 11).

Lateral-Directional Aerodynamic Characteristics

The lateral-directional aerodynamic coefficients are plotted in figures 15–21 as a function of angle of sideslip β for several angles of attack. These figures show the ranges of α and β for which the lateral-directional characteristics are linear and well behaved. Generally, all the configurations exhibit nearly linear lateral-directional behavior as a function of β for $\alpha \leq 10°$. The small nonlinearities that do occur are smooth and continuous. The body alone (fig. 15), the baseline wing-body (fig. 16), and the wing-mounted vertical-tail (fig. 19) configurations exhibit moderate nonlinearities at $\alpha = 20°$ for Mach numbers less than 3.50. The large and small centerline vertical-tail configurations (figs. 17 and 18, respectively) have highly nonlinear behavior at $\alpha = 20°$; the magnitude of these nonlinearities decreases as Mach number increases, such that at $M = 4.50$ the nonlinearities are small. The canard configurations (figs. 20 and 21) exhibit nearly linear lateral-directional characteristics at $\alpha = 20°$ for all test Mach numbers.

The lateral-directional stability derivatives, which were derived from angle-of-attack sweeps at $\beta = 0°$ and 3°, are shown in figures 22–29. The previous discussion (figs. 15–21) shows that for certain configurations (particularly the centerline vertical-tail configurations) at high angles of attack ($\alpha = 20°$), lateral-directional nonlinearities may exist. Generally, for $\beta \leq 3°$ these nonlinearities are small, but comparison of the lateral-directional stability derivatives at high angles of attack ($\alpha > 10°$) must be done cautiously.

Mach number effects on the lateral-directional stability derivatives are shown in figures 22–25. Generally, the effects of Mach number are small for $\alpha < 16°$ except for the large centerline vertical-tail configuration (fig. 24). For this configuration at $\alpha < 16°$, the magnitudes of the lateral-directional stability derivatives decrease as Mach number increases. At higher angles of attack, the results are likely affected by the previously discussed lateral-directional nonlinearities.

Lateral-directional stability characteristics are presented in figure 26 for the wing-body configuration and the three vertical-tail configurations. As expected, the wing-body with no vertical tails is directionally unstable across the Mach number and angle-of-attack range. The directional stability provided by the large and small centerline vertical tails decreases as angle of attack increases. Also, as Mach number increases, the angle of attack at which the centerline vertical-tail configurations become neutrally stable decreases. At $M = 4.50$, only the large centerline vertical-tail configuration was stable at low angles of attack (up to $\alpha = 10°$). The wing-mounted vertical tails provided a near-neutral stable configuration across the angle-of-attack and Mach number range. A larger set of wing-mounted vertical tails could provide adequate directional stability characteristics that are insensitive to angle of attack. At positive angles of attack, all configurations are laterally stable. The large and small centerline vertical tails produce the largest restoring rolling moments for $\alpha < 16°$; hence, they have greater lateral stability relative to the wing-body with no vertical tails. As the centerline verticals become shielded at high angles of attack, their effectiveness is reduced. The wing-mounted vertical configuration has the same lateral stability as the wing-body because of the offsetting effects of the upper- and lower-surface verticals. As Mach number increases, the magnitude of the lateral-directional stability derivatives decreases; hence, the incremental differences between the configurations decrease also.

The effect of canards is shown in figure 27. Generally, no canard effects occur for $\alpha < 6°$. However, the magnitude of the directional stability derivative decreases for $\alpha > 12°$, the magnitude of the side-force derivative decreases for $\alpha > 8°$, and the magnitude of the lateral-stability derivative increases slightly for $\alpha > 6°$ because of the canard addition. These canard effects generally decrease in magnitude as Mach number increases.

Wing position and wing incidence effects on the lateral-directional stability are shown in figures 28 and 29, respectively. Although the effects of wing position are small, the following trends are noted: As the wing moves forward, the absolute magnitude of

the stability derivatives (C_{n_β} and C_{l_β}) generally increases slightly; these wing position effects decrease as Mach number increases. As wing incidence is varied from negative to positive, the following general trends occur. At high angles of attack ($\alpha > 12°$) the configuration becomes more directionally unstable; this effect decreases as Mach number increases. The lateral stability increases; this effect increases as Mach number increases. Also, the negative wing incidence configurations are laterally unstable at small positive angles of attack.

Shown in figure 30 are lateral-directional data for zero angle of sideslip. At angles of attack above 20°, asymmetric loadings occur, particularly for the large centerline vertical-tail configuration. Based on similar low-speed results (refs. 2 and 3), it is believed that asymmetric vortex shedding is the cause. A review of the complete data set shows that the magnitude of the asymmetric effect decreases as Mach number increases; this is probably due to the reduced lee-side loadings imposed by vacuum pressure limitations. As Mach number increases, the asymmetry onset occurs at lower angles of attack.

Concluding Remarks

An investigation has been conducted to determine the longitudinal and lateral-directional aerodynamic characteristics of a generic wing-cone configuration at supersonic speeds. The tests were made in the Langley Unitary Plan Wind Tunnel at Mach numbers from 2.50 to 4.50. Nominal test Reynolds number was 2×10^6 per foot, with selected runs made at 1×10^6 and 4×10^6 per foot. Angle of attack was varied from $-4°$ to 28°, and angle of sideslip was varied from $-8°$ to 8°. Several configuration variables were studied to determine the effects of variations in wing longitudinal position, wing incidence, vertical-tail configuration, canard shape, and nose bluntness.

Typical effects of Reynolds number and Mach number on the longitudinal characteristics were observed. The incremental effects of the configuration variables were generally unaffected by Mach number. Forward wing shift was found to have a favorable effect on the lift and drag-due-to-lift characteristics. Wing incidence yielded nearly constant shifts in normal force, lift, and pitch at low angles of attack. The wing-mounted vertical tails increased the stability level, the normal-force-curve slope, and the lift-curve slope. Typical canard effects and minimal nose bluntness effects were observed. The baseline wing-body configuration had the greatest maximum lift-drag ratio.

Generally, all the configurations exhibited nearly linear lateral-directional characteristics for angles of attack at or below 10°. Only the large and small centerline-mounted vertical-tail configurations had significant nonlinearities at an angle of attack of 20°. The directional-stability characteristics of the large and small centerline vertical-tail configurations were significantly degraded with increasing angle of attack and Mach number. The wing-mounted vertical-tail configuration had nearly constant levels of directional stability across the test angle-of-attack range. All configurations were laterally stable for positive angles of attack except for the negative wing incidence configurations at small positive angles of attack. Lateral-directional asymmetries occurred at zero sideslip for angles of attack above 20° for the centerline vertical-tail configurations.

NASA Langley Research Center
Hampton, VA 23665-5225
March 10, 1992

References

1. Covell, Peter F.; Wood, Richard M.; Bauer, Steven X. S.; and Walker, Ira J.: *Configuration Trade and Code Validation Study on a Conical Hypersonic Vehicle.* AIAA-88-4505, Sept. 1988.

2. Luckring, James M.; Fox, Charles H., Jr.; and Cundiff, Jeffrey S.: Reynolds Number Effects on the Transonic Aerodynamics of a Slender Wing-Body Configuration. *Transonic Symposium: Theory, Application, and Experiment,* Jerome T. Foughner, Jr., compiler, NASA CP-3020, Volume II, 1989, pp. 41–58.

3. Gatlin, Gregory M.: *Low-Speed, High-Lift Aerodynamic Characteristics of Slender, Hypersonic Accelerator-Type Configurations.* NASA TP-2945, 1989.

4. Hahne, David E.; Riebe, Gregory D.; Riley, Donald R.; and Pegg, Robert J.: *Exploratory Wind-Tunnel Investigation of the Low-Speed Aerodynamic Characteristics of a Conical Aerospace Plane Concept.* NASA TP-2860, 1989.

5. Hahne, David E.; Luckring, James M.; Covell, Peter F.; Phillips, W. Pelham; Gatlin, Gregory M.; Shaughnessy, John D.; and Nguyen, Luat T.: *Stability Characteristics of a Conical Aerospace Plane Concept.* SAE Tech. Paper Ser. 892313, Sept. 1989.

6. Jackson, Charlie M., Jr.; Corlett, William A.; and Monta, William J.: *Description and Calibration of the Langley Unitary Plan Wind Tunnel.* NASA TP-1905, 1981.

7. Braslow, Albert L.; Hicks, Raymond M.; and Harris, Roy V., Jr.: *Use of Grit-Type Boundary-Layer-Transition Trips on Wind-Tunnel Models.* NASA TN D-3579, 1966.

8. Stallings, Robert L., Jr.; and Lamb, Milton: *Effects of Roughness Size on the Position of Boundary-Layer Transition and on the Aerodynamic Characteristics of a 55° Swept Delta Wing at Supersonic Speeds.* NASA TP-1027, 1977.

9. Wassum, Donald L.; and Hyman, Curtis E., Jr.: *Procedures and Requirements for Testing in the Langley Research Center Unitary Plan Wind Tunnel.* NASA TM-100529, 1988.

10. Diaconis, N. S.; Jack, John R.; and Wisniewski, Richard J.: *Boundary Layer Transition at Mach 3.12 as Affected by Cooling and Nose Blunting.* NACA TN 3928, 1957.

11. *Method for Estimating the Normal Force Coefficient of Delta Wing-Body Combinations at Supersonic Speeds at Incidences up to 25 Degrees.* Item No. 68022 (With Amendments A and B), Engineering Sciences Data Unit (London), Dec. 1987.

Table I. Geometric Characteristics of the Model

Wing W1:	
Theoretical area (reference), in^2	116.64
Aspect ratio	1.00
Span, in.	10.80
Leading-edge sweep, deg	75.96
Trailing-edge sweep, deg	0.00
Mean aerodynamic chord, in.	14.40
Airfoil section	Diamond
Airfoil thickness-to-chord ratio, percent	4.0
Vertical tail V1, body centerline:	
Exposed area, in^2	20.92
Span, in.	5.846
Leading-edge sweep, deg	70.0
Trailing-edge sweep, deg	38.13
Airfoil section	Diamond
Airfoil thickness-to-chord ratio (parallel to 9° boattail), percent	4.0
Vertical tail V2, body centerline:	
Exposed area, in^2	12.91
Span, in.	4.435
Leading-edge sweep, deg	70.0
Trailing-edge sweep, deg	−1.95
Airfoil section	Diamond
Airfoil thickness-to-chord ratio (parallel to 9° boattail), percent	4.0
Vertical tail V3, wing mounted:	
Upper surface vertical:	
Exposed area, in^2	6.46
Span, in.	2.320
Leading-edge sweep, deg	70.0
Trailing-edge sweep, deg	55.0
Airfoil section	Diamond
Airfoil thickness-to-chord ratio, percent	4.0
Lower surface vertical:	
Exposed area, in^2	5.19
Span, in.	1.800
Leading-edge sweep, deg	70.0
Trailing-edge sweep, deg	55.0
Airfoil section	Diamond
Airfoil thickness-to-chord ratio, percent	4.0

Table I. Concluded

Canard C1 (delta):	
Exposed area, in^2	5.99
Theoretical aspect ratio	1.87
Span, in.	4.50
Leading-edge sweep, deg	65.0
Trailing-edge sweep, deg	0.0
Airfoil section	Diamond
Airfoil thickness-to-chord ratio, percent	6.0
Incidence angle, deg	0.0
Canard C2 (trapezoidal):	
Exposed area, in^2	5.00
Theoretical aspect ratio	5.48
Span, in.	6.05
Leading-edge sweep, deg	16.0
Trailing-edge sweep, deg	0.0
Airfoil section	NACA 0006
Incidence angle, deg	0.0
Axisymmetric fuselage B:	
Theoretical length, in.	36.00
Forebody cone half-angle, deg	5.0
Cylinder radius (maximum), in.	2.317
Boattail half-angle, deg	9.0
Base (chamber) area, in^2	4.352
Moment reference center, in.	22.32
Radius of sharp nose (N5), in.	0.002
Radius of canard nose (N4), in.	0.010
Radius of blunt nose (N3), in.	0.124

Table II. Test Conditions

Mach number	Stagnation pressure, psi	Stagnation temperature, °F	Reynolds number, per foot
2.50	5.56	125	1×10^6
2.50	11.11	125	2
2.50	22.22	125	4
3.00	14.46	125	2
3.50	18.77	125	2
4.00	25.68	150	2
4.50	16.20	150	1
4.50	32.40	150	2
4.50	64.80	150	4

Table III. Coefficient Accuracy

The maximum absolute error of the force and moment coefficients obtained from the six-component strain-gauge balance measurements is based on, at worst case, ±0.5 percent of the full-scale balance load capability; however, based on limited data repeatability checks and the data trends, the incremental accuracy of the data is believed to be much better than that indicated by these maximum absolute error values

		Maximum absolute error for—						
M	R	C_N	C_A	C_m	C_l	C_n	C_Y	$C_{A,c}$
2.50	1×10^6	0.0090	0.0018	0.0021	0.00028	0.00112	0.0060	0.0005
2.50	2	.0045	.0009	.0010	.00014	.00056	.0030	.0003
2.50	4	.0023	.0005	.0005	.00007	.00028	.0015	.0001
3.00	2	.0052	.0010	.0012	.00016	.00064	.0035	.0003
3.50	2	.0061	.0012	.0014	.00019	.00075	.0041	.0004
4.00	2	.0068	.0014	.0016	.00021	.00084	.0045	.0004
4.50	1	.0162	.0032	.0038	.00050	.00200	.0108	.0010
4.50	2	.0081	.0016	.0019	.00025	.00100	.0054	.0005
4.50	4	.0041	.0008	.0009	.00013	.00050	.0027	.0002

Appendix

Tabulated Data

Table AI defines the symbols corresponding to the column headings of the tabulated force and moment data and the tabulated lateral-directional stability derivatives. Table AII is an index to the tabulated force and moment data, which are presented in the microfiche supplement as table AIV. Table AIII is an index to the tabulated lateral-directional stability derivatives, which are presented in the microfiche supplement as table AV.

Table AI. Symbols for Tabulated Data

Tabulated data heading	Definition
ALPHA	α
BETA	β
CA	C_A
CAC	$C_{A,c}$
CA UNC	C_A (uncorrected)
CD	C_D
CDC	$C_{D,c}$
CD UNC	C_D (uncorrected)
CL	C_L
CLB	C_l
CLS	$C_{l,s}$
CLBB	C_{l_β}
CLSB	$\left(C_{l_\beta}\right)_s$
CLSQ	C_L^2
CM	C_m
CN	C_N
CNB	C_n
CNS	$C_{n,s}$
CNBB	C_{n_β}
CNSB	$\left(C_{n_\beta}\right)_s$
CY	C_Y
CYBB	C_{Y_β}
L/D	L/D
MACH	M
R/FT	R $\times 10^{-6}$
RUN	Run number
RUNB0	$(\text{Run number})_{\beta=0^\circ}$
RUNB3	$(\text{Run number})_{\beta=3^\circ}$
XCP/L	x_{CP}/L

Table AII. Index to Tabulated Force and Moment Data

Configuration	R	α, deg	β, deg	Run number for $M =$				
				2.50	3.00	3.50	4.00	4.50
W1BN5	1×10^6	*v	0	4				61
↓	1	v	3	5				62
	1	0	v	6				63
	1	5	v	7				64
	1	10	v	8				65
	1	20	v	9				66
	2	v	0	10	27	33	41	49
	2	v	3	11	28	34	42	50
	2	0	v	15	29	36	44	51
	2	5	v	16	30	37	45	52
	2	10	v	17	31	38	46	53
	2	20	v	18	32	39	47	54
	4	v	0	20				
	4	v	3	21				
	4	0	v	22				
	4	5	v	23				
	4	10	v	24				
↓	4	20	v	25				
W1BN5V1	1×10^6	v	0					99
↓	1	v	3					100
	1	0	v					101
	1	5	v					102
	1	10	v					103
	1	20	v					104
	2	v	0	68	80	86	92	105
	2	v	3	69	81	87	93	106
	2	0	v	70	82	88	94	107
	2	5	v	71	83	89	96	108
	2	10	v	72	84	90	97	109
	2	20	v	73	85	91	98	110
	4	v	0	74				111
	4	v	3	75				112
	4	0	v	76				113
	4	5	v	77				114
	4	10	v	78				115
↓	4	20	v	79				116
W1BN5V2	2×10^6	v	0	117	123	129	136	141
↓	2	v	3	118	124	130	137	142
	2	0	v	119	125	131	138	143
	2	5	v	120	126	133	139	144
	2	10	v	121	127	134	140	145
↓	2	20	v	122	128	135	1140	146

*Variable.

Table AII. Continued

Configuration	R	α, deg	β, deg	Run number for M = 2.50	3.00	3.50	4.00	4.50
W1BN5V3	2×10^6	*v	0	159	165	171	147	153
↓	2	v	3	160	166	172	148	154
	2	0	v	161	167	173	149	155
	2	5	v	162	168	174	150	156
	2	10	v	163	169	175	151	157
	2	20	v	164	170	176	152	158
W1BN4C1	2×10^6	v	0	177	183	184	190	191
↓	2	v	3	178		185		192
	2	0	v	179		186		193
	2	5	v	180		187		194
	2	10	v	181		188		195
	2	20	v	182		189		196
W1BN4C2	2×10^6	v	0	197	203	204	210	211
↓	2	v	3	198		205		212
	2	0	v	199		206		213
	2	5	v	200		207		214
	2	10	v	201		208		215
	2	20	v	202		209		216
W1FBN5, wing forward	2×10^6	v	0	217	221	222	226	227
↓	2	v	3	218		223		228
	2	0	v	219				229
	2	5	v	220				230
W1ABN5, wing aft	2×10^6	v	0	231	235	236	240	241
↓	2	v	3	232		237		242
	2	0	v	233		238		243
	2	5	v	234		239		244
W1IBN5, $\delta_i = 5°$	2×10^6	v	0	245	253	255	263	264
↓	2	v	3	246		256		265
	2	0	v	247		257		266
	2	5	v	248		258		267
W1IBN5, $\delta_i = -5°$	2×10^6	v	0	249	254	259	262	268
↓	2	v	-3	250		260		269
	2	0	v	251		257		
	2	-5	v	252		261		270
W1IBN5, $\delta_i = 2.5°$	2×10^6	v	0	271	279	282	289	290
↓	2	v	3	272		281		291
	2	0	v	273		283		292
W1IBN5, $\delta_i = -2.5°$	2×10^6	v	0	275	278	285	288	294
↓	2	v	-3	276		286		295
	2	-5	v	277		287		296

*Variable.

Table AII. Concluded

Configuration	R	α, deg	β, deg	Run number for $M =$				
				2.50	3.00	3.50	4.00	4.50
W1BN3	2×10^6	*v	0	297	301	302	306	307
↓	2	v	3	298		303		308
	2	0	v	299		304		309
	2	5	v	300		305		310
BN5	1×10^6	v	0	311				331
↓	2	v	0	312	319	321	328	332
	2	v	3	313	320	322	329	333
	2	0	v	314		323		334
	2	5	v	315		324		335
	2	10	v	316		327		336
	2	20	v	317		326		337
	4	v	0	318				338

*Variable.

Table AIII. Index to Tabulated Lateral-Directional Stability Derivatives

Configuration	R	Run number ($\beta = 0°/\beta = 3°$) for $M =$				
		2.50	3.00	3.50	4.00	4.50
W1BN5	1×10^6	4/5				61/62
W1BN5	2	10/11	27/28	33/34	41/42	49/50
W1BN5	4	20/21				
W1BN5V1	1					99/100
W1BN5V1	2	68/69	80/81	86/87	92/93	105/106
W1BN5V1	4	74/75				111/112
W1BN5V2	2	117/118	123/124	129/130	136/137	141/142
W1BN5V3	2	159/160	165/166	171/172	147/148	153/154
W1BN5C1	2	177/178		184/185		191/192
W1BN5C2	2	197/198		204/205		211/212
W1FBN5	2	217/218		222/223		227/228
W1ABN5	2	231/232		236/237		241/242
W1IBN5, $\delta_i = 5°$	2	245/246		255/256		264/265
W1IBN5, $\delta_i = -5°$	2	249/250		259/260		268/269
W1IBN5, $\delta_i = 2.5°$	2	271/272		281/282		290/291
W1IBN5, $\delta_i = -2.5°$	2	275/276		285/286		294/295
W1BN3	2	297/298		302/303		307/308
BN5	2	312/313	319/320	321/322	328/329	332/333

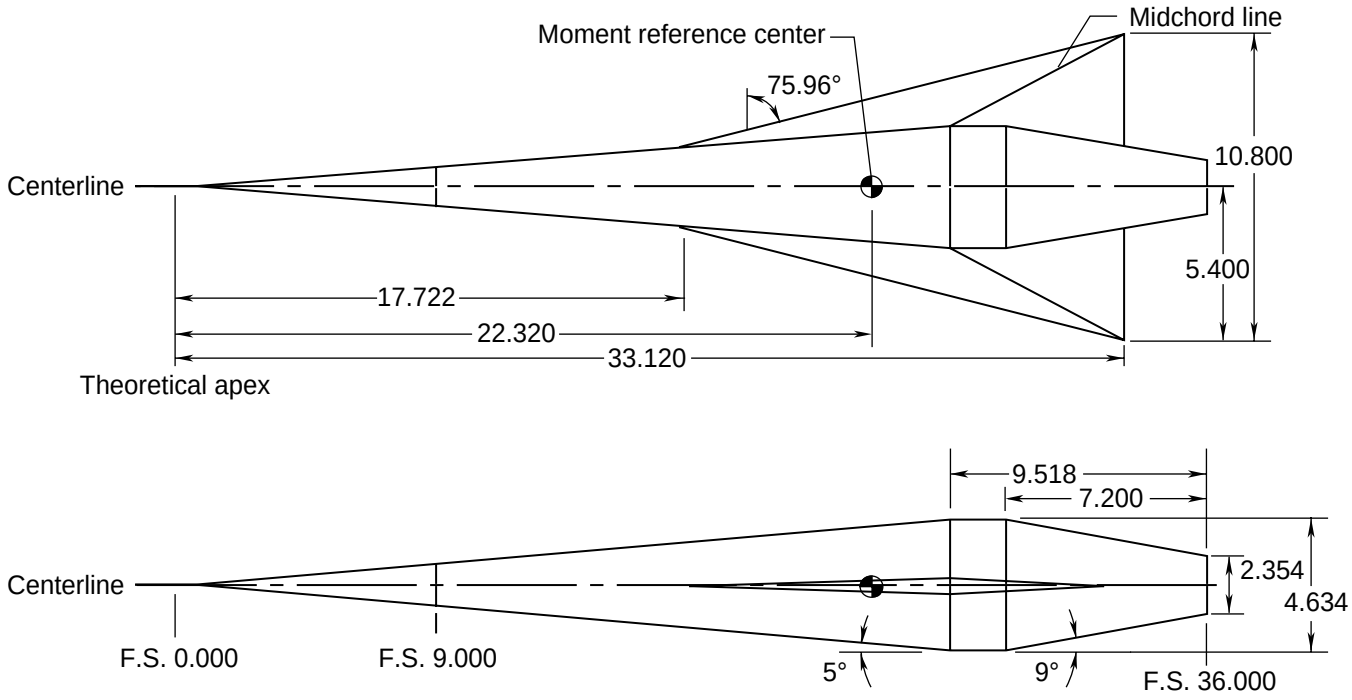

(a) General arrangement of the model. Wing in baseline (mid) position at zero incidence.

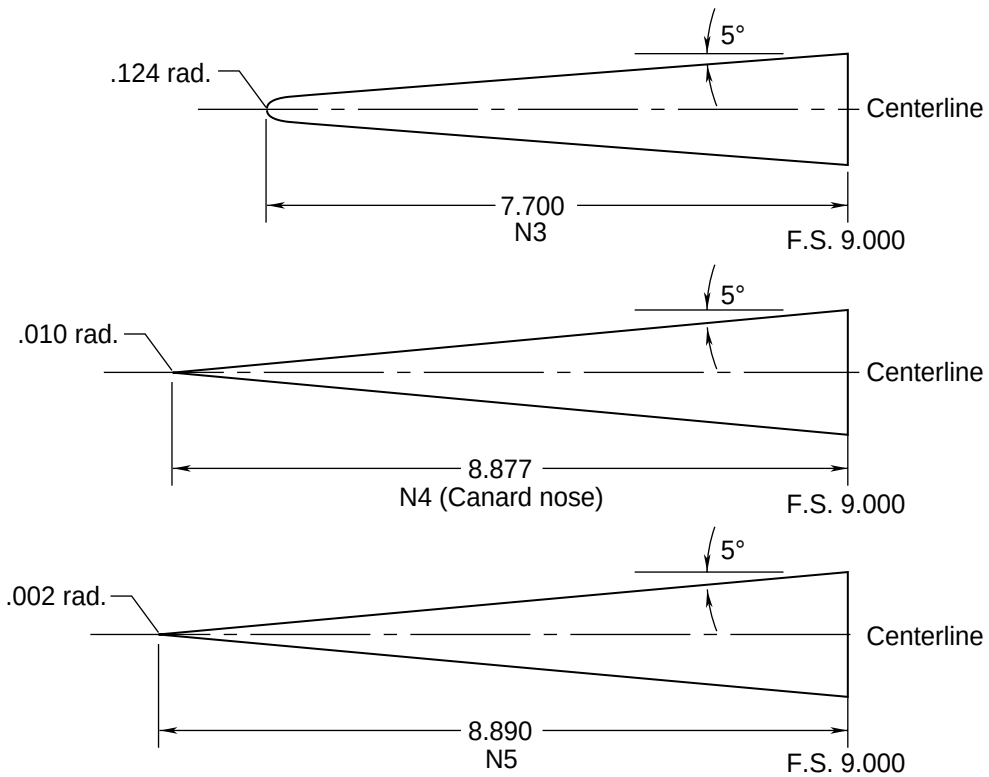

(b) Details of the fuselage nose.

Figure 1. Geometric description of wind-tunnel model. All dimensions are given in inches.

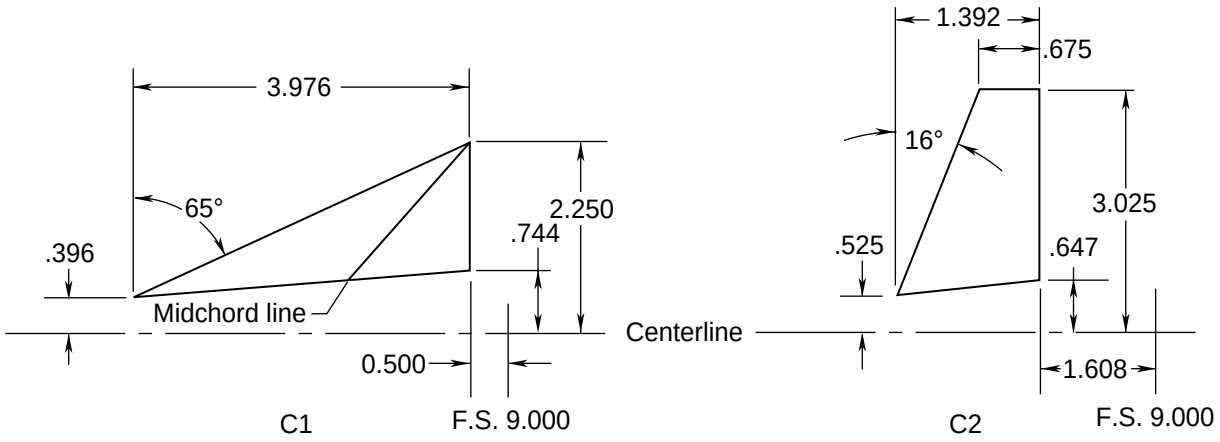

(c) Canard details.

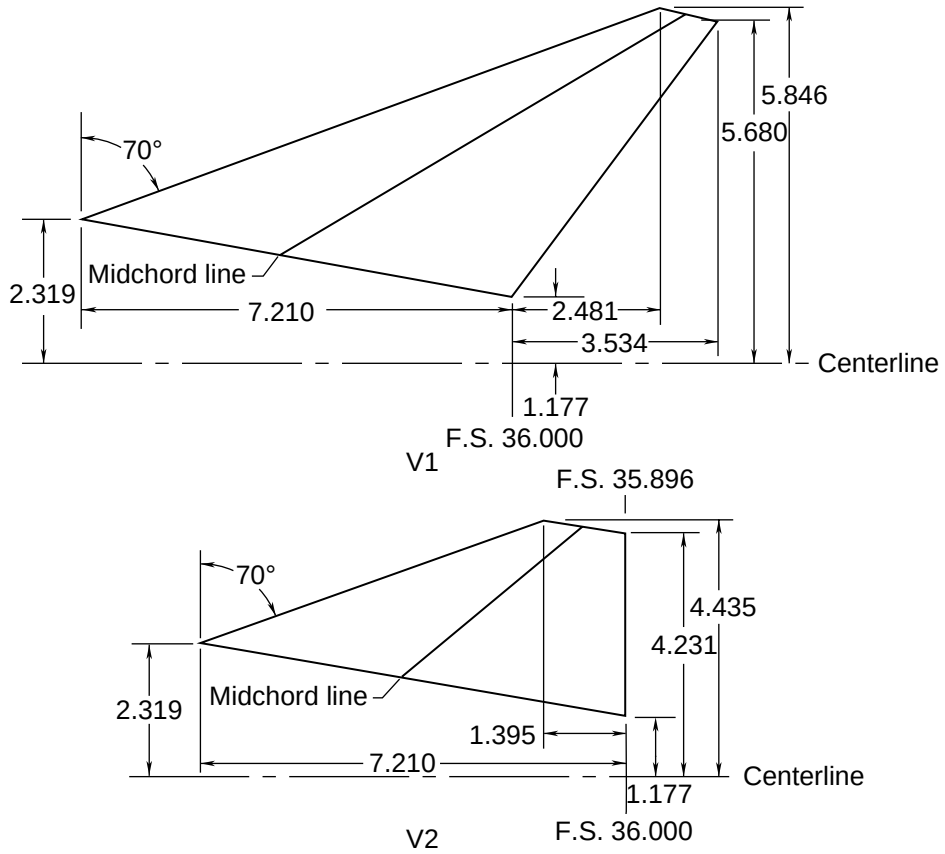

(d) Details of centerline-mounted vertical tails.

Figure 1. Continued.

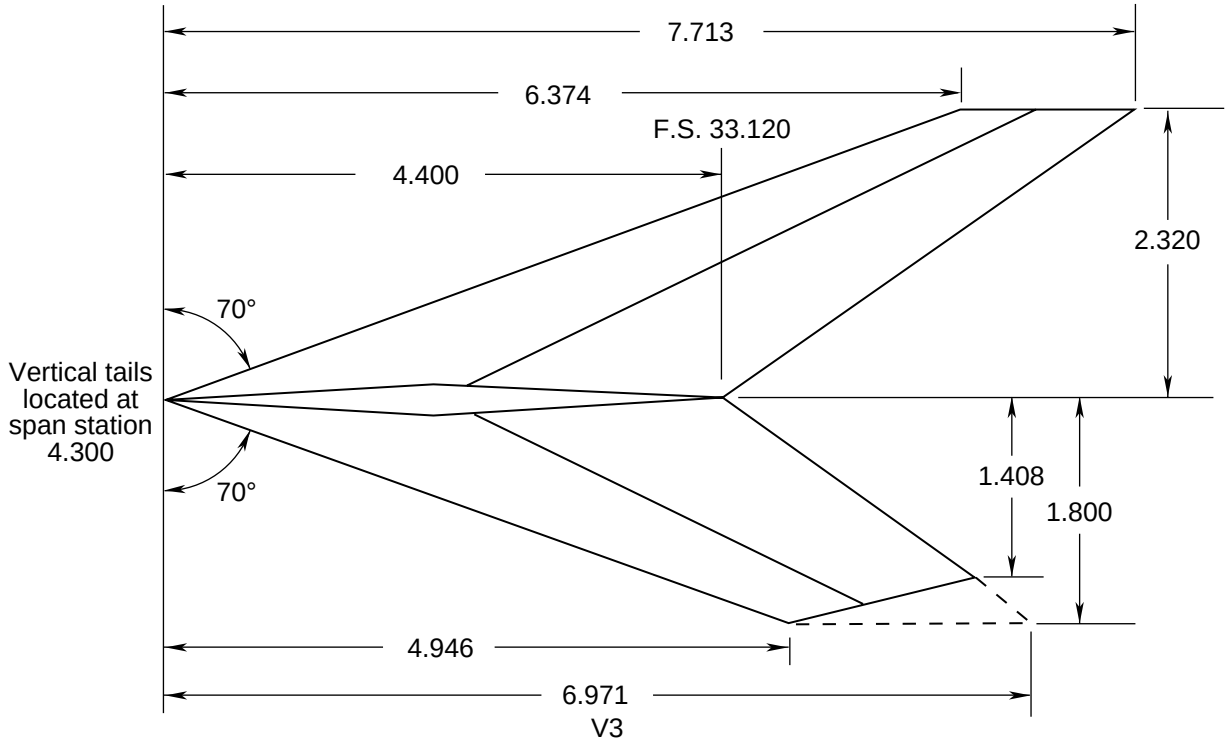

(e) Details of wing-mounted vertical tail.

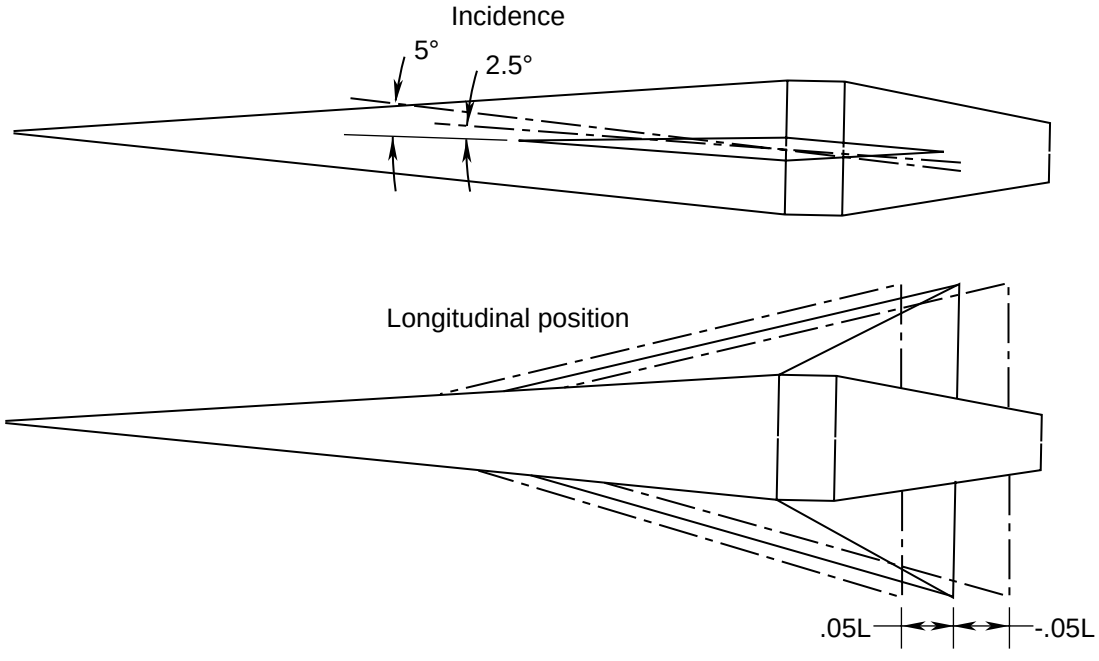

(f) Wing incidence and position variables.

Figure 1. Concluded.

(c) Canard details.

(d) Details of centerline-mounted vertical tails.

Figure 1. Continued.

L-87-11, 172

Figure 2. Photograph of model mounted in Test Section 2 of Unitary Plan Wind Tunnel; W1BN5V1 configuration.

(a) $M = 2.50$.

Figure 3. Effect of Reynolds number on longitudinal aerodynamic characteristics; BN5.

(a) Continued.

Figure 3. Continued.

(a) Concluded.

Figure 3. Continued.

(b) $M = 4.50$.

Figure 3. Continued.

(b) Continued.

Figure 3. Continued.

(b) Concluded.

Figure 3. Concluded.

Figure 4. Effect of Reynolds number on longitudinal aerodynamic characteristics; W1BN5; $M = 2.50$.

Figure 4. Continued.

Figure 4. Concluded.

(a) $M = 2.50$.

Figure 5. Effect of Reynolds number on longitudinal aerodynamic characteristics; W1BN5V1.

(a) Continued.

Figure 5. Continued.

(a) Concluded.

Figure 5. Continued.

(b) $M = 4.50$.

Figure 5. Continued.

(b) Continued.

Figure 5. Continued.

(b) Concluded.

Figure 5. Concluded.

Figure 6. Effect of Mach number on longitudinal aerodynamic characteristics; BN5.

Figure 6. Continued.

Figure 6. Concluded.

Figure 7. Effect of Mach number on longitudinal aerodynamic characteristics; W1BN5.

Figure 7. Continued.

Figure 7. Concluded.

Figure 8. Effect of Mach number on longitudinal aerodynamic characteristics; W1BN5V1.

Figure 8. Continued.

Figure 8. Concluded.

Figure 9. Effect of Mach number on longitudinal aerodynamic characteristics; W1BN4C1.

Figure 9. Continued.

Figure 9. Concluded.

(a) $M = 2.50$.

Figure 10. Effect of vertical tail on longitudinal aerodynamic characteristics; W1BN5.

(a) Continued.

Figure 10. Continued.

(a) Concluded.

Figure 10. Continued.

(b) $M = 3.00$.

Figure 10. Continued.

(b) Continued.

Figure 10. Continued.

(b) Concluded.

Figure 10. Continued.

(c) $M = 3.50$.

Figure 10. Continued.

(c) Continued.

Figure 10. Continued.

(c) Concluded.

Figure 10. Continued.

(d) $M = 4.00$.

Figure 10. Continued.

(d) Continued.

Figure 10. Continued.

(d) Concluded.

Figure 10. Continued.

(e) $M = 4.50$.

Figure 10. Continued.

(e) Continued.

Figure 10. Continued.

(e) Concluded.

Figure 10. Concluded.

(a) $M = 2.50$.

Figure 11. Effect of canard on longitudinal aerodynamic characteristics; W1BN5 for canard off; W1BN4 for canard on.

(a) Continued.

Figure 11. Continued.

(a) Concluded.

Figure 11. Continued.

(b) $M = 3.00$.

Figure 11. Continued.

(b) Continued.

Figure 11. Continued.

(b) Concluded.

Figure 11. Continued.

(c) $M = 3.50$.

Figure 11. Continued.

(c) Continued.

Figure 11. Continued.

(c) Concluded.

Figure 11. Continued.

(d) $M = 4.00$.

Figure 11. Continued.

(d) Continued.

Figure 11. Continued.

(d) Concluded.

Figure 11. Continued.

(e) $M = 4.50$.

Figure 11. Continued.

(e) Continued.

Figure 11. Continued.

(e) Concluded.

Figure 11. Concluded.

(a) $M = 2.50$.

Figure 12. Effect of wing position on longitudinal aerodynamic characteristics; W1BN5.

(a) Continued.

Figure 12. Continued.

(a) Concluded.

Figure 12. Continued.

(b) $M = 3.00$.

Figure 12. Continued.

(b) Continued.

Figure 12. Continued.

(b) Concluded.

Figure 12. Continued.

(c) $M = 3.50$.

Figure 12. Continued.

(c) Continued.

Figure 12. Continued.

(c) Concluded.

Figure 12. Continued.

(d) $M = 4.00$.

Figure 12. Continued.

(d) Continued.

Figure 12. Continued.

(d) Concluded.

Figure 12. Continued.

(e) $M = 4.50$.

Figure 12. Continued.

(e) Continued.

Figure 12. Continued.

(e) Concluded.

Figure 12. Concluded.

(a) $M = 2.50$.

Figure 13. Effect of wing incidence on longitudinal aerodynamic characteristics; W1IBN5.

(a) Continued.

Figure 13. Continued.

(a) Concluded.

Figure 13. Continued.

(b) $M = 3.00$.

Figure 13. Continued.

(b) Continued.

Figure 13. Continued.

(b) Concluded.

Figure 13. Continued.

(c) $M = 3.50$.

Figure 13. Continued.

(c) Continued.

Figure 13. Continued.

(c) Concluded.

Figure 13. Continued.

(d) $M = 4.00$.

Figure 13. Continued.

(d) Continued.

Figure 13. Continued.

(d) Concluded.

Figure 13. Continued.

(e) $M = 4.50$.

Figure 13. Continued.

(e) Continued.

Figure 13. Continued.

(e) Concluded.

Figure 13. Concluded.

(a) $M = 2.50$.

Figure 14. Effect of nose bluntness on longitudinal aerodynamic characteristics.

(a) Continued.

Figure 14. Continued.

(a) Concluded.

Figure 14. Continued.

(b) $M = 3.00$.

Figure 14. Continued.

(b) Continued.

Figure 14. Continued.

(b) Concluded.

Figure 14. Continued.

(c) $M = 3.50$.

Figure 14. Continued.

(c) Continued.

Figure 14. Continued.

(c) Concluded.

Figure 14. Continued.

(d) $M = 4.00$.

Figure 14. Continued.

(d) Continued.

Figure 14. Continued.

(d) Concluded.

Figure 14. Continued.

(e) $M = 4.50$.

Figure 14. Continued.

(e) Continued.

Figure 14. Continued.

(e) Concluded.

Figure 14. Concluded.

(a) $M = 2.50$.

Figure 15. Effect of angle of attack on lateral-directional aerodynamic characteristics; BN5.

(b) $M = 3.50$.

Figure 15. Continued.

(c) $M = 4.50$.

Figure 15. Concluded.

(a) $M = 2.50$.

Figure 16. Effect of angle of attack on lateral-directional aerodynamic characteristics; W1BN5.

(b) $M = 3.00$.

Figure 16. Continued.

(c) $M = 3.50$.

Figure 16. Continued.

(d) $M = 4.00$.

Figure 16. Continued.

(e) $M = 4.50$.

Figure 16. Concluded.

(a) $M = 2.50$.

Figure 17. Effect of angle of attack on lateral-directional aerodynamic characteristics; W1BN5V1.

(b) $M = 3.00$.

Figure 17. Continued.

(c) $M = 3.50$.

Figure 17. Continued.

(d) $M = 4.00$.

Figure 17. Continued.

(e) $M = 4.50$.

Figure 17. Concluded.

(a) $M = 2.50$.

Figure 18. Effect of angle of attack on lateral-directional aerodynamic characteristics; W1BN5V2.

(b) $M = 3.00$.

Figure 18. Continued.

(c) $M = 3.50$.

Figure 18. Continued.

(d) $M = 4.00$.

Figure 18. Continued.

(e) $M = 4.50$.

Figure 18. Concluded.

(a) $M = 2.50$.

Figure 19. Effect of angle of attack on lateral-directional aerodynamic characteristics; W1BN5V3.

(b) $M = 3.00$.

Figure 19. Continued.

(c) $M = 3.50$.

Figure 19. Continued.

(d) $M = 4.00$.

Figure 19. Continued.

(e) $M = 4.50$.

Figure 19. Concluded.

(a) $M = 2.50$.

Figure 20. Effect of angle of attack on lateral-directional aerodynamic characteristics; W1BN4C1.

(b) $M = 3.50$.

Figure 20. Continued.

(c) $M = 4.50$.

Figure 20. Concluded.

(a) $M = 2.50$.

Figure 21. Effect of angle of attack on lateral-directional aerodynamic characteristics; W1BN4C2.

(b) $M = 3.50$.

Figure 21. Continued.

(c) $M = 4.50$.

Figure 21. Concluded.

Figure 22. Effect of Mach number on lateral-directional stability derivatives; BN5.

Figure 23. Effect of Mach number on lateral-directional stability derivatives; W1BN5.

Figure 24. Effect of Mach number on lateral-directional stability derivatives; W1BN5V1.

Figure 25. Effect of Mach number on lateral-directional stability derivatives; W1BN4C1.

(a) $M = 2.50$.

Figure 26. Effect of vertical tail on lateral-directional stability derivatives; W1BN5.

(b) $M = 3.00$.

Figure 26. Continued.

(c) $M = 3.50$.

Figure 26. Continued.

(d) $M = 4.00$.

Figure 26. Continued.

(e) $M = 4.50$.

Figure 26. Concluded.

(a) $M = 2.50$.

Figure 27. Effect of canard on lateral-directional stability derivatives; W1BN5 for canard off; W1BN4 for canard on.

(b) $M = 3.50$.

Figure 27. Continued.

(c) $M = 4.50$.

Figure 27. Concluded.

(a) $M = 2.50$.

Figure 28. Effect of wing position on lateral-directional stability derivatives; W1BN5.

(b) $M = 3.50$.

Figure 28. Continued.

(c) $M = 4.50$.

Figure 28. Concluded.

(a) $M = 2.50$.

Figure 29. Effect of wing incidence on lateral-directional stability derivatives; W1IBN5.

(b) $M = 3.50$.

Figure 29. Continued.

(c) $M = 4.50$.

Figure 29. Concluded.

(a) $M = 2.50$.

Figure 30. Effect of vertical tail on lateral-directional asymmetric effects at $\beta = 0°$; W1BN5.

(b) $M = 3.00$.

Figure 30. Continued.

(c) $M = 3.50$.

Figure 30. Continued.

(d) $M = 4.00$.

Figure 30. Continued.

(e) $M = 4.50$.

Figure 30. Concluded.